Nanoscale

PAPER

View Article Online
View Journal | View Issue

Cite this: *Nanoscale*, 2018, **10**, 23175

The interplay between Zeeman splitting and spin–orbit coupling in InAs nanowires†

Bum-Kyu Kim,‡[a] Sang-Jun Choi,‡[b,c] Jae Cheol Shin,‡[d] Minsoo Kim,[e] Ye-Hwan Ahn,[a,f] H.-S. Sim,*[b] Ju-Jin Kim*[g] and Myung-Ho Bae *[a,h]

Received 22nd September 2018,
Accepted 14th November 2018

DOI: 10.1039/c8nr07728b

rsc.li/nanoscale

Coupling of the electron orbital motion and spin, *i.e.*, spin–orbit coupling (SOC) leads to nontrivial changes in energy-level structures, giving rise to various spectroscopies and applications. The SOC in solids generates energy-band inversion or splitting under zero or weak magnetic fields, which is required for topological phases or Majorana fermions. Here, we examined the interplay between the Zeeman splitting and SOC by performing the transport spectroscopy of Landau levels (LLs) in indium arsenide nanowires under a strong magnetic field. We observed the anomalous Zeeman splitting of LLs, which depends on the quantum number of LLs as well as the electron spin. We considered that this observation was attributed to the interplay between the Zeeman splitting and the SOC. Our findings suggest an approach of generating spin-resolved chiral electron transport in nanowires.

Introduction

Landau orbitals, circular motions of an electron in a two-dimensional electron gas (2DEG) under a magnetic field, have discrete energy values known as Landau levels (LLs). These levels are further split when the spin and valley degrees of freedom come into play, or due to variations in the number of layers in the case of graphene or electron–electron interactions.[1–5] Spectroscopy of LLs has provided valuable information, with the splitting patterns suggesting the possibility of new phases of matter. In addition to the factors mentioned above, the interplay between the Rashba spin–orbit coupling (RSOC) and Zeeman effects also leads to generate interesting splitting of the LLs. Here, the RSOC originates from the breaking of structural inversion symmetry along the direction perpendicular to the 2D plane.[6] Indeed, in InGaAs/InAlAs 2DEG systems, Shubnikov–de Haas oscillations, precursors to LLs, exhibit a beating pattern under a weak magnetic field that has been attributed to this interplay.[7] However, obtaining direct evidence of the splitting of LLs caused by the interplay has proved challenging because the strength of the RSOC fluctuates markedly over the 2DEG,[8] smearing the discrete energy spectra. Recent transport experiments, in which a narrow 2DEG region is formed in indium arsenide (InAs) nanowires with strong RSOC when a gate voltage is applied, have overcome this issue,[6,9–11] allowing the observation of the Zeeman splitting of LLs under a strong magnetic field.[9,10] However, the interplay between RSOC and Zeeman effects remains unexplored.[11]

Here we report the experimental features of the Zeeman splitting dressed by the RSOC of LLs in InAs nanowires under a strong magnetic field. First, we confirm that a strong magnetic field can form LLs in the narrow 2DEG on the top of such nanowires, which is induced by a back-gate voltage[9–13] at a temperature of 50 K. Second, on lowering the temperature to 35 K, our transport spectroscopy revealed that the LLs split in an anomalous fashion; the spin Zeeman splitting of the lowest LL is observed to be larger than that of the second-lowest LL. The result is attributed to the interplay between the Zeeman splitting and RSOC in the InAs nanowires. Finally, we show that the experimental results agree with a numerical simulation based on a narrow 2DEG formed in an InAs nanowire.

[a]*Korea Research Institute of Standards and Science, Daejeon 34113, Republic of Korea. E-mail: mhbae@kriss.re.kr*
[b]*Department of Physics, Korea Advanced Institute of Science and Technology, Daejeon 34141, Republic of Korea. E-mail: hssim@kaist.ac.kr*
[c]*Center for Theoretical Physics of Complex Systems, Institute for Basic Science, Daejeon 34126, Republic of Korea*
[d]*Department of Physics, Yeungnam University, Gyeongsan 38541, Republic of Korea*
[e]*Department of Physics, Pohang University of Science and Technology, Pohang 790-784, Republic of Korea*
[f]*Department of Physics, Korea University, Seoul 136-713, Republic of Korea*
[g]*Department of Physics, Chonbuk National University, Jeonju 561-756, Republic of Korea. E-mail: jujinkim@chonbuk.ac.kr*
[h]*Department of Nano Science, University of Science and Technology, Daejeon, 34113, Republic of Korea*

†Electronic supplementary information (ESI) available. See DOI: 10.1039/c8nr07728b

‡These authors contributed equally to this work.

Results and discussion

Preparation of InAs nanowire devices

The InAs nanowires used in this study were grown in a catalyst-free metalorganic chemical vapor deposition system with a horizontal reactor (A200/AIXTRON Inc.). A 2 inch Si(111) wafer was cleaned with a buffered oxide etchant for 1 min and rinsed in deionized (DI) water for 5 s. Then, the wafer was dipped in poly-L-lysine solution (Sigma-Aldrich Inc.) for 2 min and rinsed in DI water for 10 s. The wafer was then loaded into the MOCVD reactor. To grow the nanowires, the reactor pressure was lowered to 50 mbar with 15 L min^{-1} of hydrogen gas flow and the reactor temperature was increased to 570 °C. After a short stabilization time, arsine gas (AsH_3) was flowed into the reactor for 1 min, followed by trimethylindium (TMIn). The molar flow rates of TMIn and AsH_3 were 2×10^{-5} and 2×10^{-4} mol min^{-1}, respectively. Nanowire growth was performed for 90 min, which was the time required to form 20 μm tall InAs nanowires. The morphologies of the InAs nanowires were investigated by scanning electron microscopy (SEM, Hitachi-S4700, Hitachi Inc.). The structural properties of the InAs nanowires were examined by transmission electron microscopy (JEM-2200FS, JEOL Inc). The nanowires exhibit a zinc-blende crystal structure but a large number of stacking faults was observed along the nanowire growth direction (*i.e.* ⟨111⟩) as shown in the inset of Fig. 1a. Nevertheless, no misfit dislocation was found across the InAs nanowire. The X-ray diffraction analysis was also performed as shown in section 1 in the ESI.† The nanowires have nearly uniform heights of ~20 μm with a diameter of ~90 nm with well-controlled growth conditions such as temperature and growth time (see Fig. 1a).

To fabricate the InAs nanowire FETs, as-grown InAs nanowires were first dispersed in isopropanol by sonication for 10 s, and then dispersed on a highly doped silicon substrate covered with a 300 nm thick oxide layer with pre-patterned metal markers. The highly doped silicon substrate was used as the global back-gate electrode. The multi-terminal electrodes were defined by standard electron-beam lithography and electron-beam evaporation of Ti/Au (10/150 nm). Prior to metal deposition, the native oxide layer on the InAs nanowire surface was etched in 2% diluted solution of 3 M ammonium polysulfide $(NH_4)_2S_x$ at 60 °C for 5 min to achieve a low contact resistance. For the electrical measurements, the differential conductance was measured using a standard lock-in amplifier (SR830) with an excitation voltage of 100 μV and a frequency of 1.777 kHz superimposed on a DC bias voltage (Yokogawa 7651) in a physical property measurement system (PPMS).

Fig. 1b shows the prepared InAs field-effect transistors (FETs), where the upper and lower panels display SEM images of the devices with a length (L) and diameter (D) of ~85 nm and ~70 nm, respectively (NW1), and ~160 nm and ~85 nm, respectively (NW2). The measurement configuration is overlaid on the upper panel of Fig. 1b. The field-effect mobility was estimated as ~2500 cm^2 V^{-1} s^{-1} for a 3 μm-long-channel at T = 5 K, which was consistent with our previous report.[14] Charge depletion by the back-gate voltage V_g gives rise to the formation of a narrow 2DEG at the top of the channel (see hexahedral region marked with red dashes in Fig. 1c).[9–13] Our numerical simulation showed that a sufficiently thin channel with an arch shaped potential can be formed near the middle of the ~80 nm long channel under a relevant V_g condition (see section 2 of the ESI†).

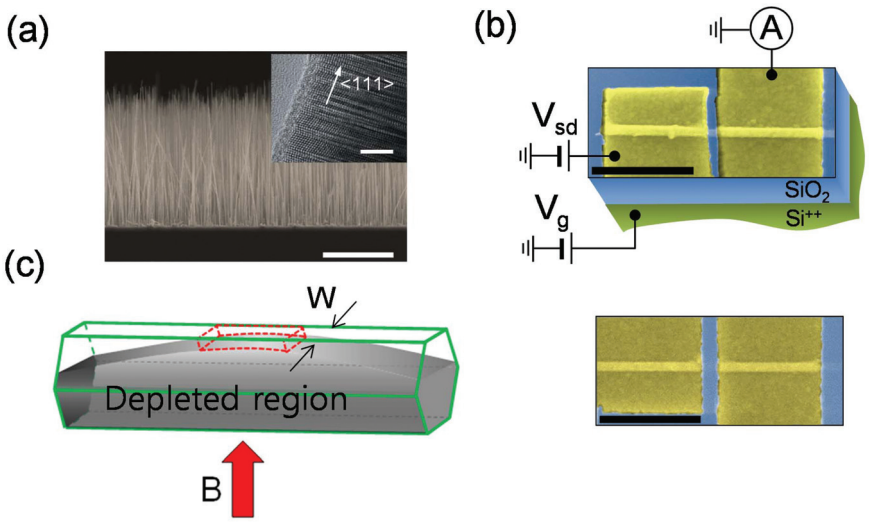

Fig. 1 (a) Scanning electron microscopy (SEM) image of grown InAs nanowires on a Si(111) wafer, which shows nearly uniform heights of ~20 μm with a diameter of ~90 nm. Scale bar is 10 μm. Inset: A high-resolution transmission electron microscopy image of a grown InAs nanowire. Scale bar is 5 nm. (b) Upper and lower panels: False-colored SEM images of NW1 and NW2, respectively. Scale bars: 1 μm. Yellow regions indicate that metal electrodes and InAs channels are located between them. The upper panel shows an overlaid measurement configuration. (c) Charge depletion of an InAs nanowire by the electric field induced by a back-gate voltage. The green frame depicts the outline of the nanowire, and metal electrodes are located at the ends of the channel. The grey region represents the charge depletion region, and the red box indicates the region where a quasi-2DEG is formed. Here, '*W*' denotes the width of the 2DEG region. A perpendicular magnetic field *B* is applied to the nanowire.

Landau levels in InAs nanowires

For sample NW1, magnetic fields from 0 T to 9 T were applied perpendicular to the substrate (see Fig. 1c) at T = 50 K. Such high temperature was needed to suppress the Fabry–Pérot interference, allowing us to clearly discern the conductance steps (also see section 3 of the ESI† for the Fabry–Pérot interference).[15] Fig. 2a shows the zero-bias conductance of NW1 as a function of the gate voltage (G–V_g curves) for various magnetic-field (B) values. As the field strength was increased, a conductance plateau emerged near $G \sim 0.7$ from B = 4 T, and it became wider as the field was increased to B = 9 T (see red dotted box in Fig. 2a). To reveal the origin of the conductance plateau, we examined a dG/dV_g map of NW1 as a function of V_{sd} and V_g with increasing B (see Fig. 2b). The dG/dV_g map exhibited a diamond structure (dashed lines) from which information on the energy levels could be extracted (*cf.* Fig. 3d). The ΔV_{sd} corresponding to the energy level spacing is proportional to the magnetic field, as indicated in Fig. 2c by squares (diamonds) for sample NW1 (NW2). Here, measurements for sample NW2 were conducted at the lower temperature of 35 K. This indicates that the diamond structure does not originate from Fabry–Pérot interference or quantum dot effects, for which the energy scales are relatively insensitive to the magnetic field strength.[16] We also note that Zeeman splitting is not the full origin of the conductance plateau observed in Fig. 2. Considering the energy-change amount of ~12 meV when the field varies from 6 T to 9 T

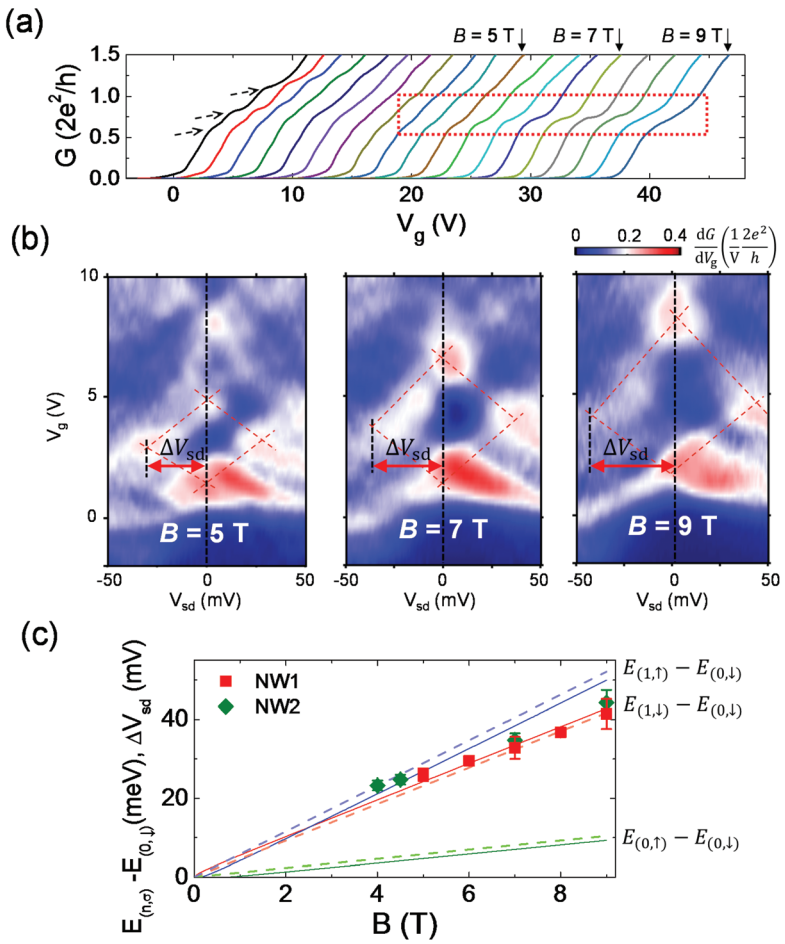

Fig. 2 (a) G–V_g curves for the ~85 nm-long device (NW1) at various B-fields perpendicular to the substrate from zero (leftmost) to 9 T (rightmost) with the interval of 0.5 T at T = 50 K. Data are horizontally shifted for clarity. Dashed arrows indicate step-like conductance structures observed at B = 0 T that become smeared out with increasing B-field. These structures are interpreted as the Fabry–Pérot interference (see section 3 of the ESI†).[33] A conductance step near $G \sim 0.7$ emerged at B = 4 T, which evolves into an apparent step at B = 9 T (see the region enclosed by a dashed red box). This is interpreted as a signature of the formation of the LLs in the nanowire. (b) dG/dV_g as a function of V_{sd} and V_g at B = 5, 7 and 9 T (from left to right), which shows diamond structures (dashed lines). Here, ΔV_{sd} corresponds to the LL spacing $E_{(1,\downarrow)} - E_{(0,\downarrow)}$. (c) ΔV_{sd} as a function of magnetic field, whereby scattered square and diamond points were obtained from NW1 and NW2, respectively. The error bar at each field was obtained by considering ΔV_{sd} values for both polarities of V_{sd}. The energy difference of $E_{n\downarrow} = E_{n\downarrow} - E_{0\downarrow}$, obtained from eqn (1), is drawn as dashed and solid lines for regimes (ii) and (iii) in Fig. 3, respectively. The experimental data of ΔV_{sd} are in agreement with the difference for B > 5 T, where the magnetic length, l_B is comparable to the nanowire width so that LLs can be well developed.

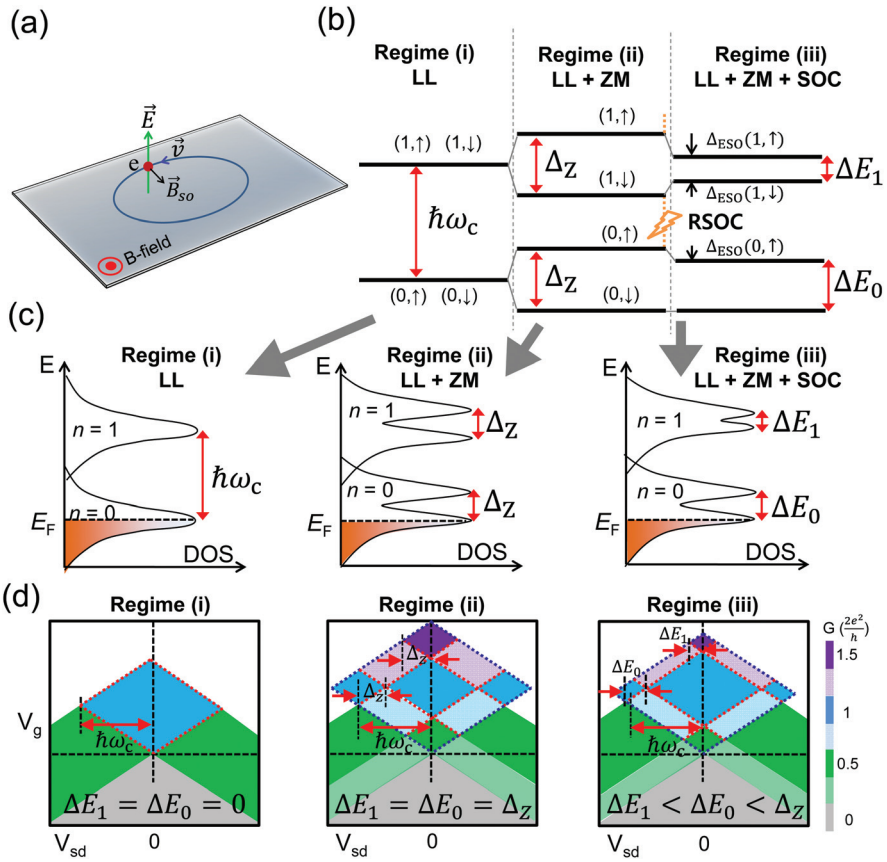

Fig. 3 (a) Landau orbit of an electron in a 2DEG on an *xy* plane under a perpendicular magnetic field, $\boldsymbol{B} = B\hat{\boldsymbol{z}}$. The Landau orbital is affected by the Zeeman effect of a Hamiltonian $H_{ZM} \propto \boldsymbol{B}\cdot\boldsymbol{\sigma}$ and the RSOC of $H_{SO} \propto \boldsymbol{B}_{SO}\cdot\boldsymbol{\sigma}$, where $\boldsymbol{B}_{SO} \propto \boldsymbol{v} \times \boldsymbol{E}$ is the effective magnetic field induced by the RSOC, σ is the electron spin, $\boldsymbol{v}$ is the electron velocity, and $\boldsymbol{E}$ is the electric field induced by a back-gate voltage. (b) Splitting of LLs of the 2DEG in the three regimes: (i) bare LLs with a cyclotron frequency, ω_c, (ii) LL + ZM (LL splitting by Zeeman energy Δ_Z) and (iii) LL + ZM + SOC (LL splitting by the Zeeman effect and the RSOC in a strong *B*). Electron states (n, σ) are characterized by the LL orbital quantum number n and spin quantum number σ. ΔE_0 and ΔE_1 are the energy splittings of n = 0 and n = 1 LLs, respectively, and $\Delta_{ESO}(n, \sigma)$ is the effective RSOC energy in the regime (iii). (c) Schematic DOS of the two lowest LLs (n = 0, 1) of a 2DEG in the three regimes. The DOS shows the spin splitting energies of Δ_Z, ΔE_0, and ΔE_1. (d) Expected conductance maps of the two lowest LLs (n = 0, 1) of a 2DEG in the three regimes. The map shows the two-terminal conductance G of the 2DEG as a function of V_{sd} and V_g. From the size of the diamond structures in the map, one can identify the spin splitting energies of Δ_Z, ΔE_0, and ΔE_1.

(see Fig. 2c), g should be ~70 with a relation of $\Delta_Z = g\mu_B B$, where Δ_Z is the Zeeman energy, g is the Landé g-factor and μ_B is the Bohr magneton. Recent reports[17,18] have indicated that the orbital motion around the approximately cylindrical surface of a nanowire can give rise to huge Landé g-factor values (as high as 50); however, this effect does not occur under a perpendicular magnetic field with respect to the nanowire axis, and hence cannot be the source of the plateau.[18] To explain the B-field dependent energy scale, we consider the LL occurring in a 2DEG system with B-field. To do that, we construct a theoretical model including LL, Zeeman splitting and SOC as mentioned below.

Theoretical model for interplay between Zeeman splitting and SOC in the Landau regime

Landau orbitals of an electron in a 2DEG under a strong perpendicular magnetic field are affected by Zeeman and RSOC effects (see Fig. 3a and b). In this case, the energy levels of the electron are as follows (see section 4 in the ESI†):

$$E_{(n,\sigma)} \approx \left(n + \frac{1}{2}\right)\hbar\omega_c + \sigma\frac{\Delta_Z}{2} - \sigma\Delta_{ESO}(n,\sigma),$$
$$\Delta_{ESO}(n,\sigma) \equiv \frac{2(2n+\sigma+1)}{1-\dfrac{\Delta_Z}{\hbar\omega_c}}\Delta_{SO}, \quad (1)$$

where n (= 0, 1, 2, ...) is the quantum number of the n-th LL, $\hbar$ is the reduced Planck constant, $\omega_c = eB/m^*$ is the cyclotron frequency, m^* is the electron effective mass, e is the electron charge, and σ (= +1, −1 for spin state ↑, ↓, respectively) is the quantum number of the electron spin. The final term, $\Delta_{ESO}(n, \sigma)$, is the effective RSOC term correcting the Zeeman splitting energy, which is proportional to the RSOC

energy $\Delta_{SO} \equiv \frac{m^* \alpha^2}{2\hbar^2}$, where α is the RSOC strength. Notice that $\Delta_{ESO}(n, \sigma)$ depends on both the LL quantum number n and the electron spin σ, and the interplay between the Zeeman and RSOC effects enhance the strength of Δ_{ESO} by a factor of $1/\left(1 - \frac{\Delta_Z}{\hbar\omega_c}\right)$ as shown in its analytical expression.

Fig. 3b shows the energy levels $E_{(n,\ \sigma)}$ determined using eqn (1) in different regimes: (i) no SOC and Zeeman effects ($\Delta_{SO} = \Delta_Z = 0$), (ii) with only the Zeeman effect ($\Delta_{SO} = 0$, $\Delta_Z \neq 0$), and (iii) with both SOC and Zeeman effects ($\Delta_{SO} \neq 0$, $\Delta_Z \neq 0$). In regime (i), the LLs are not split $\Delta E_1 = \Delta E_0 = 0$, where $\Delta E_n \equiv E_{(n,\ \uparrow)} - E_{(n,\ \downarrow)}$ denotes the level splitting of the n-th LL. In regime (ii), the Zeeman effect lifts the spin degeneracy of levels $(n, \uparrow)$ and $(n, \downarrow)$ by the same amount Δ_Z, *i.e.*, $\Delta E_1 = \Delta E_0 = \Delta_Z$. In regime (iii), by contrast, the effective SOC causes LL-dependent Zeeman splitting $\Delta E_1 < \Delta E_0 < \Delta_Z$. The RSOC triggers level splitting between $(n + 1, \downarrow)$ and $(n, \uparrow)$ so that $\Delta_{ESO}(n, \sigma)$ makes $\Delta E_n \left(= \Delta_Z - \frac{2(2n+1)}{1 - \frac{\Delta_Z}{\hbar\omega_c}} \Delta_{SO} \right)$ smaller than the bare Zeeman splitting Δ_Z (see Fig. 3b), and the $\Delta_{ESO}(n, \sigma)$ becomes stronger for higher LLs.

Experimentally, the information of LL splitting can be extracted from transport spectroscopy, an approach that has been found useful for various systems.[9,19–22] Fig. 3c and d conceptually show the electron density of states (DOS) and the resulting two-terminal electron conductance $G(V_g, V_{sd})$, respectively. Here, the three columns of panels correspond to regimes (i)–(iii), respectively. The Fermi energy E_F is tuned by V_g. Each spin-resolved LL gives rise to a jump by $G_0/2 \equiv e^2/h$ in the conductance as a function of V_g whenever the Fermi energy crosses the LL (*e.g.*, see the horizontal dashed lines in regimes (ii) and (iii) of Fig. 3c).[23] A conductance jump also occurs whenever another LL is allowed to start contributing to the conductance by increasing the source–drain bias voltage V_{sd}. As a result, diamond patterns appear in the conductance map $G(V_g, V_{sd})$ (Fig. 3d). As denoted in Fig. 3d by red arrows, information on the energy gaps (*e.g.*, ΔE_n) can be derived from the diamond pattern. Thus, by using transport spectroscopy, one can identify the Zeeman splitting dressed by the SOC of LLs.

Now, we compare the experimental data of Fig. 2b with eqn (1) in Fig. 2c. The solid lines in Fig. 2c depicted the LL spacing depending on the B field, where the solid red line indicates the energy difference between the second and first LLs, $E_{(1,\downarrow)} - E_{(0,\ \downarrow)}$, based on the parameter values of $\alpha \sim 0.36$ eV Å, $g = 20$ and $m^* = 0.025 m_e$. Here, m_e is the rest mass of a free electron.[6,24–27] The energy level spacing ΔV_{sd} with the B field for two devices shows good agreement with the calculated line. This agreement indicates that the conductance steps observed in the G–V_g curves for $B > 5$ T in Fig. 2a originate from the LLs, in accordance with the results of previous experiments on nanowires under strong magnetic fields.[9–11] In the absence of a magnetic field, the FET dimension corresponds to a multiband one-dimensional nanowire. However, under a high magnetic field, the strong Lorentz force hybridizes the multiple subbands; the magnetic length ($l_B = 26\,\text{nm}/\sqrt{B[T]}$) is 13 nm at 4 T, shorter than the lateral width ($W \sim 40$ nm in Fig. 1c) or the radius of the nanowire. This also supports the formation of the LLs. To obtain further evidence of this behavior in our system, we compared the energy scales and conducted a numerical simulation (described in section 4 of the ESI†). We note that the normalized conductance value corresponding to the conductance step was ~0.7, not 1, because the 2DEG exists partly in the middle of the channel, with inevitable contact resistance. In addition, a partial charge depletion in the nanowire occurred in the positive V_g region, which can happen when the Fermi level of an InAs nanowire is located near the conduction band edge.[12,20,28] Because of the thermal broadening, the results in Fig. 2b lack the resolution required to discern the spin splitting of LLs, making it impossible to determine if the system is in regime (i), (ii) or (iii). Below we discuss the spin splitting behaviour at a lower temperature.

Interplay between the Zeeman splitting and the SOC

To elucidate the interplay between the Zeeman splitting and the SOC in the LLs, we conducted transport spectroscopy of NW2 at $T = 35$ K. For $T < 30$ K, it was hard to distinguish the conductance steps from the Fabry–Pérot interference (see Fig. S4a†). In the dG/dV_g map obtained at $B = 9$ T (Fig. 4a), the blue-colored diamond pattern contains a sub-structure (dashed red lines) indicating the spin splitting of LLs (also see Fig. S6† for the G–V_g curves at various B-fields). The energy splitting of the lowest LL ($n = 0$) extracted from Fig. 4a is $\Delta E_0 \sim 12 \pm 1$ meV. The splitting is larger than the thermal broadening by $k_B T \sim 3$ meV, and comparable to the value $\Delta E_0 \sim 9.4$ meV theoretically estimated using eqn (1) with the parameter values mentioned above. In contrast, the expected energy splitting of the next LL ($n = 1$) indicated by ΔE_1 in Fig. 4a was not shown. It is predicted that the second lowest LL ($n = 1$) has a smaller energy splitting of roughly $\Delta E_1 \sim 7$ meV with eqn (1), which is comparable to the thermal broadening. This could be a reason why we could not observe the energy splitting at $n = 1$ LL. To clarify the origin of the level splitting, we conducted a numerical simulation of the dG/dV_g map in a narrow 2DEG with a width (W) of 44 nm, as depicted in Fig. 1c, under $B = 9$ T, where a series resistance (R_s) of 10 kΩ was assumed (see section 3 of the ESI†). The left and right panels of Fig. 4b show the simulation results obtained for regimes (ii) and (iii) in Fig. 3b, respectively (see also Fig. 3d). The left panel of Fig. 4b shows identical amounts of energy splitting Δ_Z for both $n = 0$ and $n = 1$ LLs. However, in the right panel of Fig. 4b, the energy splitting of $n = 1$ LL (ΔE_1) has almost disappeared, whereas ΔE_0 is still visible. Thus, we consider that the transport spectroscopy data (Fig. 4a) agree with regime (iii) with the SOC effect.

Moreover, the level splitting features were further identified as peak–dip–peak behaviors in the $dG/dV_g - V_g$ curves at $V_{sd} =$

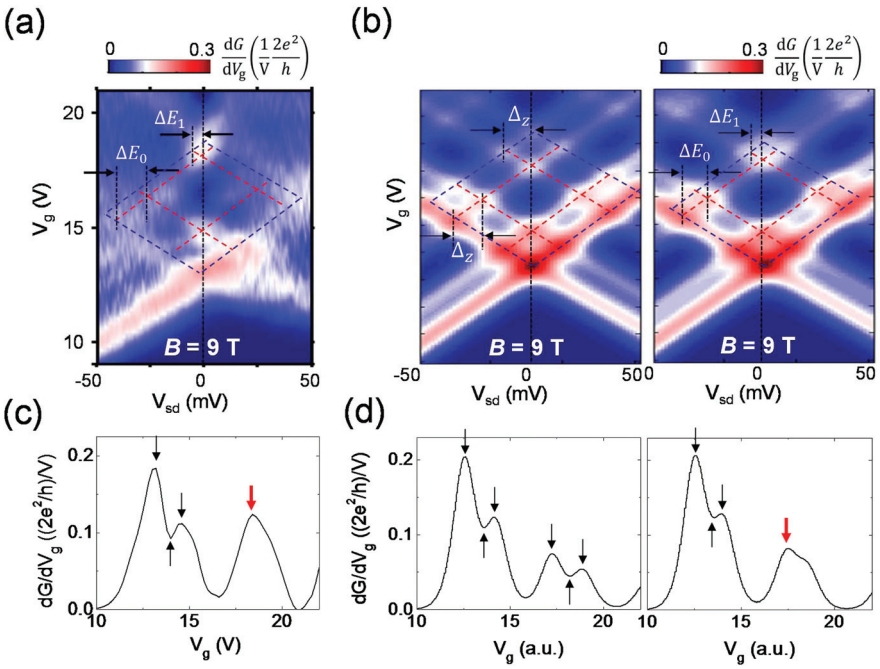

Fig. 4 (a) dG/dV_g map as a function of V_{sd} and V_g of NW2 at B = 9 T and T = 35 K. The diamond structure is depicted by the dashed blue lines, and its sub-structure is indicated by dashed red lines. (b) The left and right panels show the numerical calculation of the dG/dV_g map as a function of V_{sd} and V_g in regimes (ii) and (iii) in Fig. 3(d), respectively, for an InAs 2DEG system under B = 9 T at T = 35 K. We used parameters of W = 44 nm, $\alpha \sim$ 0.36 eV A, g = 20 and m^* = 0.025m_e. The blue- and red-dashed lines and the notations for the energy scales correspond to those in regimes (ii) and (iii) shown in Fig. 3(d). (c) $dG/dV_g - V_g$ curves obtained by slicing the dG/dV_g map in (a) at V_{sd} = 0 mV. (d) Left and right panels: $dG/dV_g - V_g$ curves obtained from the left and right panels of (b), respectively, at V_{sd} = 0 mV. The downward and upward arrows in (c) and (d) indicate dG/dV_g peaks and dips, respectively.

0 mV. The $dG/dV_g - V_g$ curves in Fig. 4c and d were obtained experimentally and theoretically along dashed vertical lines in Fig. 4a and b, respectively. Here, the left and right panels in Fig. 4d were obtained from the left and right panels in Fig. 4b, respectively. The left panel in Fig. 4d shows two successive peak–dip–peak groups with the same peak-to-peak spacing, which corresponds to the bare Zeeman splitting of the LLs. By contrast, the right panel in Fig. 4d shows a single peak–dip–peak feature and another separate peak indicated by a red arrow. The first peak–dip–peak feature has the peak-to-peak spacing corresponding to the splitting ΔE_0 of the lowest LL. The second single peak indicated by a red arrow originates from the thermal broadening of a peak–dip–peak structure of the peak-to-peak spacing ΔE_1 of the second lowest LL. This feature in the right panel of Fig. 4d is consistent with the experimental data in Fig. 4c (see the second single peak indicated by a red arrow), which is compatible with the interplay between the Zeeman splitting and SOC; the spin Zeeman splitting ΔE_0 of the lowest LL is larger than the ΔE_1 of the second-lowest LL. In addition, we note that the interplay between the Zeeman and SOC effects has enhanced the strength of ΔE_n by a factor of 1.4, as previously mentioned in the theoretical model section. Without the enhancement, ΔE_0 and ΔE_1 are diminished into $\Delta E_0 \sim 8$ meV and $\Delta E_1 \sim 5$ meV, respectively, which cannot present the peak–dip–peak behaviors demonstrated in our experiment.

Conclusion

We used transport spectroscopy data to elucidate the interplay between the Zeeman splitting and SOC in the Landau regime in a narrow 2DEG formed in InAs nanowires by applying a back-gate voltage. This spectroscopy could be also applied to other nanowires with strong SOC, such as a Bi_2Se_3 topological insulator.[29–32] Our findings, showing LL splitting in a 2DEG formed in InAs nanowires, suggest that under strong magnetic fields nanowires may exhibit new phenomena such as spin-resolved quantum Hall effects or spin-resolved chiral electron transport.

Conflicts of interest

There are no conflicts to declare.

Acknowledgements

This work was supported by the Korea Research Institute of Standards and Science (KRISS-GP2018-003), part of the Basic Science Research Program through the National Research Foundation of Korea (NRF) (Grant No. 2018R1A2A1A05078440, SRC2016R1A5A1008184, NRF-2016R1A2B4008525 and

NRF-2017R1C1B2010906). This work was also partly supported by the Korea-Hungary Joint Laboratory Program for Nanosciences through the National Research Council of Science and Technology.

References

1 Y. Zhang, Y.-W. Tan, H. L. Stormer and P. Kim, *Nature*, 2005, **438**, 201–204.
2 K. S. Novoselov, E. McCann, S. V. Morozov, V. I. Fal'ko, M. I. Katsnelson, U. Zeitler, D. Jiang, F. Schedin and A. K. Geim, *Nat. Phys.*, 2006, **2**, 177–180.
3 T. Taychatanapat, K. Watanabe, T. Taniguchi and P. Jarillo-herrero, *Nat. Phys.*, 2011, **7**, 621–625.
4 Y. Xu, I. Miotkowski, C. Liu, J. Tian, H. Nam, N. Alidoust, J. Hu, C.-K. Shih, M. Z. Hasan and Y. P. Chen, *Nat. Phys.*, 2014, **10**, 956–963.
5 S. Ilani, J. Martin, E. Teitelbaum, J. H. Smet, D. Mahalu, V. Umansky and A. Yacoby, *Nature*, 2004, **427**, 328–332.
6 A. Manchon, H. C. Koo, J. Nitta, S. M. Frolov and R. A. Duine, *Nat. Mater.*, 2015, **14**, 871–882.
7 J. Nitta, T. Akazaki, H. Takayanagi and T. Enoki, *Phys. Rev. Lett.*, 1997, **78**, 1335–1338.
8 J. R. Bindel, M. Pezzotta, J. Ulrich, M. Liebmann, E. Y. Sherman and M. Morgenstern, *Nat. Phys.*, 2016, **12**, 920–925.
9 S. Heedt, W. Prost, J. Schubert, D. Grützmacher and T. Schäpers, *Nano Lett.*, 2016, **16**, 3116–3123.
10 S. Heedt, A. Manolescu, G. A. Nemnes, W. Prost, J. Schubert, D. Grutzmacher and T. Schapers, *Nano Lett.*, 2016, **16**, 4569–4575.
11 S. Heedt, N. T. Ziani, F. Crépin, W. Prost, S. Trellenkamp, J. Schubert, D. Grützmacher, B. Trauzettel and T. Schäpers, *Nat. Phys.*, 2017, **13**, 563–568.
12 I. van Weperen, S. R. Plissard, E. P. A. M. Bakkers, S. M. Frolov and L. P. Kouwenhoven, *Nano Lett.*, 2013, **13**, 387–391.
13 V. E. Degtyarev, S. V. Khazanova and N. V. Demarina, *Sci. Rep.*, 2017, **7**, 3411.
14 J. C. Shin, A. Lee, H. J. Kim, J. H. Kim, K. J. Choi, Y. H. Kim, N. Kim, M.-H. Bae, J.-J. Kim and B.-K. Kim, *J. Korean Phys. Soc.*, 2013, **62**, 1678–1682.
15 A. V. Kretinin, R. Popovitz-Biro, D. Mahalu and H. Shtrikman, *Nano Lett.*, 2010, **10**, 3439–3445.
16 L. L. Sohn, L. P. Kouwenhoven and G. Schön, *Mesoscopic Electron Transport*, 1997.
17 S. M. Albrecht, A. P. Higginbotham, M. Madsen, F. Kuemmeth, T. S. Jespersen, J. Nygård, P. Krogstrup and C. M. Marcus, *Nature*, 2016, **531**, 206–209.
18 G. W. Winkler, D. Varjas, R. Skolasinski, A. A. Soluyanov, M. Troyer and M. Wimmer, *Phys. Rev. Lett.*, 2017, **119**, 37701.
19 W. Lu, J. Xiang, B. P. Timko, Y. Wu and C. M. Lieber, *Proc. Natl. Acad. Sci. U. S. A.*, 2005, **102**, 10046–10051.
20 Y. Tian, M. R. Sakr, J. M. Kinder, D. Liang, M. J. Macdonald, R. L. J. Qiu, H.-J. Gao and X. P. A. Gao, *Nano Lett.*, 2012, **12**, 6492–6497.
21 A. C. Ford, S. B. Kumar, R. Kapadia, J. Guo and A. Javey, *Nano Lett.*, 2012, **12**, 1340–1343.
22 S. Abay, D. Persson, H. Nilsson, H. Q. Xu, M. Fogelström, V. Shumeiko and P. Delsing, *Nano Lett.*, 2013, **13**, 3614–3617.
23 S. Datta, *Electronic transport in mesoscopic systems*, Cambridge University Press, 1997.
24 S. E. Hernández, M. Akabori, K. Sladek, C. Volk, S. Alagha, H. Hardtdegen, M. G. Pala, N. Demarina, D. Grützmacher and T. Schäpers, *Phys. Rev. B: Condens. Matter Mater. Phys.*, 2010, **82**, 235303.
25 D. Liang and X. P. A. Gao, *Nano Lett.*, 2012, **12**, 3263–3267.
26 A. Das, Y. Ronen, Y. Most, Y. Oreg, M. Heiblum and H. Shtrikman, *Nat. Phys.*, 2012, **8**, 887–895.
27 V. Y. Aleshkin, V. I. Gavrilenko, A. V. Ikonnikov, S. S. Krishtopenko, Y. G. Sadofyev and K. E. Spirin, *Semiconductors*, 2008, **42**, 828–833.
28 F. Vigneau, V. Prudkovkiy, I. Duchemin, W. Escoffier, P. Caroff, Y. M. Niquet, R. Leturcq, M. Goiran and B. Raquet, *Phys. Rev. Lett.*, 2014, **112**, 76801.
29 M. Z. Hasan and C. L. Kane, *Rev. Mod. Phys.*, 2010, **82**, 3045–3067.
30 X. L. Qi and S. C. Zhang, *Rev. Mod. Phys.*, 2011, **83**, 1057–1110.
31 J. Alicea, *Rep. Prog. Phys.*, 2012, **75**, 76501.
32 P. D. C. King, R. C. Hatch, M. Bianchi, R. Ovsyannikov, C. Lupulescu, G. Landolt, B. Slomski, J. H. Dil, D. Guan, J. L. Mi, E. D. L. Rienks, J. Fink, A. Lindblad, S. Svensson, S. Bao, G. Balakrishnan, B. B. Iversen, J. Osterwalder, W. Eberhardt, F. Baumberger and P. Hofmann, *Phys. Rev. Lett.*, 2011, **107**, 96802.
33 L. C. Campos, A. F. Young, K. Surakitbovorn, K. Watanabe, T. Taniguchi and P. Jarillo-Herrero, *Nat. Commun.*, 2012, **3**, 1239.